

Received 25 October 2023; revised 27 November 2023; accepted 7 December 2023. Date of publication 29 December 2023; date of current version 26 March 2024.

Digital Object Identifier 10.1109/OJAP.2023.3348188

# True-Time-Delay Metasurface Assisted Broadband and Planarized Resonant Cavity Antenna

TAYYAB A. KHAN<sup>1</sup> (Member, IEEE), AND ALEX M. H. WONG<sup>2</sup> (Senior Member, IEEE)

<sup>1</sup>Department of Electrical Engineering, City University of Hong Kong, Hong Kong

<sup>2</sup>State Key Laboratory of Terahertz and Millimeter Waves, Department of Electrical Engineering, City University of Hong Kong, Hong Kong

CORRESPONDING AUTHOR: A. M. H. WONG (e-mail: alex.mh.wong@cityu.edu.hk)

This work was supported by the Early Career Scheme from the Research Grants Council of Hong Kong under Grant 21211619.

This article has supplementary downloadable material available at <https://doi.org/10.1109/OJAP.2023.3348188>, provided by the authors.

**ABSTRACT** Resonant cavity antennas (RCAs) produce reasonably high gains (15-20 dBi) with thin form factors, and find strong applications in wireless communication. A recently proposed RCA achieves a broad 3dB bandwidth of over 20% using a spherically modified ground (SMG), but its curved metallic surface is very costly to manufacture at high frequencies. In this paper, we planarize this broadband RCA by replacing the SMG with a true-time-delay metasurface (TTD-MS) which mimics the both reflection phase shift and time-delay of the SMG over antenna's entire operation bandwidth. We verify our proposed method through full-wave simulations and experimental measurements. Our measurements demonstrate an impedance bandwidth ( $S_{11} \leq -10$  dB) of 32% and a 3dB-gain bandwidth of 21.3% (from 11.95 GHz to 14.8 GHz), with a peak gain of 17.5 dBi. This performance is comparable to the RCA with the SMG, but we have planarized the structure, leading to dramatic simplification in fabrication. The height of the cavity is also reduced by 20%. The proposed TTD-MS RCA exhibits high gain, stable impedance matching, reduced cavity height and simple configuration, and elucidates a new path to RCA design for microwave and mm-wave frequencies.

**INDEX TERMS** Fabry-Pérot antennas, leaky-wave antennas, resonant cavity antennas, metasurfaces.

## I. INTRODUCTION

HIGH gain antennas are the backbone of modern-day communication systems. Traditionally, high-gain performance for such systems relied on parabolic reflectors and phased array antennas [1]. However, the fabrication challenges associated with the curved shape of parabolic reflectors, the limited ability of these reflectors to scan electronic beams at wide angles, and the substantial cost associated with phased array antennas has created a significant need for alternative solutions for modern day applications. Accordingly, several classes of high-gain antennas have emerged, which, in varying ways, mitigate the disadvantages associated with parabolic and phased array antennas. These include reflectarrays, folded reflectarrays, transmitarrays, and resonant cavity antennas (RCAs), among many others [1].

Despite the attractive features of reflect and transmit array antennas, such as their planar structure, cost-effectiveness,

and ability to produce narrow radiated beams, they also come with limitations. These include a restricted bandwidth, potential feed blockage (in the case of reflectarrays), and a large longitudinal/vertical antenna profile: the spatial feeding mechanism in these antennas with a focal length ( $F$ ) distance between the primary feed and the reflect or transmit array apertures tends to be large, and is often comparable to or larger than the lateral size of the antenna [1]. The antenna profile, in particular, is critical for developing contemporary compact communication systems. Therefore, the concepts of folded reflect- and transmit- arrays have emerged, reducing the antenna height to  $F/2$  and  $F/3$ , respectively [2], [3], [4], [5], [6], [7], [8]. Several recent works demonstrated folded reflectarrays with heights of several wavelengths ranging from  $3\lambda_0$  to  $5\lambda_0$  [2], [4], [5], [6], [7], [8]. They achieve such reduction by employing a polarization-conversion surface and a polarizer, spaced  $F/2$  apart, with a primary source

embedded along the axis of the polarization conversion surface. While the introduction of polarization conversion surface is instrumental in the working of folded reflectarray, it also alters the polarization of the primary source. Thus, the outgoing waves from the folded reflectarrays are of orthogonal polarization to the feed wave. Moreover, most folded reflectarrays are single-polarized since the polarizer is used to achieve the desired reflection/transmission control.

Concurrently with the development of folded reflectarrays, researchers investigated another class of antennas, known as RCAs, to demonstrate their ability to achieve highly directive radiation performance using more compact structures. RCAs, also known as Fabry-Pérot antennas or a type of leaky-wave antennas, have received significant attention in recent years due to their ability to offer directive radiation characteristics with a simple configuration [9], [10], [11], [12]. In contrast to the previously mentioned high-gain antenna systems, the RCA exhibits several attractive features. Firstly, the cavity height of the RCA is typically a multiple of the half wavelength, i.e.,  $n\frac{\lambda}{2}$  (where  $n = 1, 2, \dots$ ), resulting in a low-profile and compact design. Secondly, the feeding mechanism employed in the RCA streamlines its design by eliminating the need for phase shifters and power dividers to establish the in-phase radiating fields. Such an implementation approach mitigates the additional feed losses, which are inevitable in certain high-gain antenna systems. The compact design, along with the simplified feeding mechanism, reduces the overall cost of the system. Therefore, due to its advantageous characteristics, including high-gain performance, low-profile design, and cost-effectiveness, the use of RCAs is of great importance in modern-day technological applications such as imaging systems, long-range communication, sensor networks, and electronic warfare, among others [13], [14], [15], [16].

The basic configuration of an RCA, as shown in Fig. 1(a), comprises a primary feeding source (e.g., a waveguide or a dipole antenna) embedded inside the cavity formed by a metallic ground plane and a partially reflecting surface (PRS) [9], [10]. The PRS can be designed using single or multiple dielectric slabs [17], [18], [19], [20], [21], [22], [23], frequency selective surfaces (FSS) [24], [25], [26], or 3D woodpile structure [27]. Several analytical methods such as ray tracing technique [9], leaky-wave theory [28], and electromagnetic band gap analysis [29] have been established in the literature to accurately predict the radiation characteristics of the RCA. According to the ray-tracing method, at the Fabry-Pérot condition, the operating frequency of the RCA is given as:

$$f = \frac{c}{4\pi h_c} (\phi_{\text{PRS}} + \phi_{\text{GND}} - 2N\pi) \quad N = 0, 1, 2, \dots \quad (1)$$

where  $c$  is the speed of light in free space ( $2.997 \times 10^8$  m/s), and  $\phi_{\text{PRS}}$  and  $\phi_{\text{GND}}$ , respectively, represent the reflection phases of the PRS and the ground plane, and  $h_c$  is the cavity height. From (1), we note that the Fabry-Pérot condition is

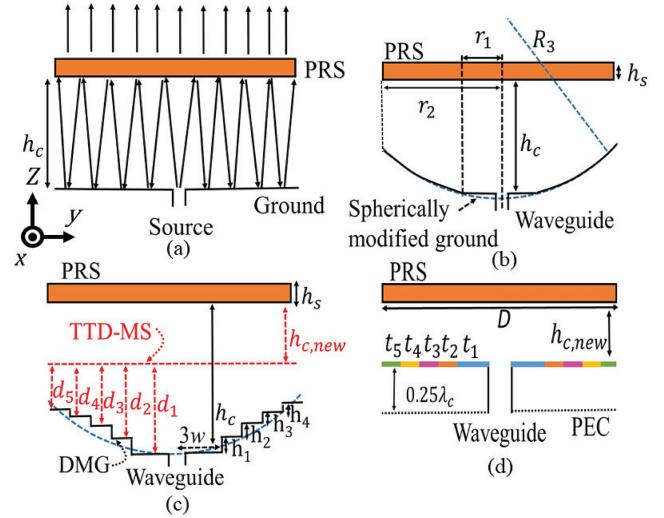


**FIGURE 1.** Different configurations of the resonant cavity antenna (RCA).

(a) Conventional RCA design. (b) RCA with a spherically modified ground [14]. Dimensions are  $r_1 = 1.16\lambda_c$ ,  $r_2 = 2.80\lambda_c$ ,  $h_s = 0.283\lambda_g$ ,  $\lambda_g = 6.70$ ,  $h_c = 1.16\lambda_c$ ,  $R_3 = 12.62\lambda_c$ . (c) RCA with a discretized modified ground (black); The red text and labels indicate the location of the true-time-delay metasurface (TTD-MS) that will be implemented. (d) A schematic showing the proposed RCA with a TTD-MS placed inside the cavity at  $h_{c,new} = 0.69\lambda_c$ . The proposed RCA has a diameter of  $D = 5.22\lambda_c$ ; All units are in (mm);  $\lambda_c$  is free space wavelength at 14 GHz.

satisfied for a discrete set of frequencies. This limits the RCA to a narrow working bandwidth surrounding the resonance frequencies.

To this end, researchers have put forward solutions to enhance the 3dB-gain bandwidth of the RCA, mainly by adopting three different approaches. In the first approach, antenna arrays are applied as an excitation of the RCA to achieve uniform illumination of the cavity, thereby enhancing the gain bandwidth product (GBP) and aperture efficiency [30], [31], [32], [33]. For example, a multisource feeding technique was utilized in [33], and a 3dB-gain enhancement of 14% with a maximum gain of 22.5 dB was achieved. Although incorporating more sources inside the cavity enhances the radiation performance of the RCA, it adds to the design complexity, and cost, and introduces losses due to feeding networks. In the second approach, specially designed PRS's with positive phase gradients (positive slope versus frequency) [15], [23], [24], [25], [26], [34], [35], multilayer dielectric slabs [21], [23], [36], [37], [38] and stepped dielectric slabs [13], [39], have been applied to enhance the 3dB-gain bandwidth of the RCA. Especially, the RCA designs with smaller footprints demonstrate their capability to achieve wideband performance with large gain bandwidths [13], [39]. However, the utilization of multilayer superstructures to achieve such performance complicates the fabrication and increases the overall antenna height and weight. The third approach involves reshaping the ground plane of an RCA [14], [40], [41], [42], [43], [44], [45]. Reference [14] demonstrates that replacing the flat ground with the spherically modified ground (SMG) (refer to Fig. 1(b)) helps to excite the fundamental as well as higher-order cavity modes known as Quasi-Laguerre-Gaussian

(QLG) beam modes, ultimately realizing a high gain over a wide bandwidth. Although the SMG utilizes a single metallic layer, the overall height of the cavity is approximately  $1\lambda_0$  (where  $\lambda_0$  is the wavelength in free space at the lower frequency of the working band), which hinders its integration in compact systems. Also, manufacturing such a modified ground requires precise machining and control techniques, which adds complexity to the design process, especially at higher frequencies. References [44], [45] somewhat relax the fabrication complexities at higher frequencies by introducing multilayer planar grounds to approximate the reflection of a spherical ground. However, this method also introduces its own fabrication complexity as it involves multilayer PCB cutting and bonding.

In this paper, we propose a wideband RCA whereby the SMG of [14] is replaced by a planar metasurface that mimics its reflection properties. To achieve this, a planar metasurface with spatially varying properties is employed. This metasurface should be designed in such a way that each unit-cell possesses identical reflection phase shift and time-delay characteristics as the corresponding section of the SMG that it replaces. Previous works [46], [47], [48], [49], [50], [51], [52] have shown that a true-time-delay metasurface (TTD-MS) can achieve a stable time delay over a wide bandwidth. Implementing the TTD-MS with the required time delay and reflection phase at one design frequency will result in a metasurface replacement for the SMG. Thereafter, combining the designed metasurface with the PRS layer will result in a planarized TTD-MS RCA with excellent broadband performance.

Section II of this paper briefly reviews the design of an RCA using a SMG and a discretized modified ground (DMG). Section III discusses the design and physical realization of a TTD-MS that approximates the performance of the DMG in the previous section. Sections IV and V report the simulation results and experimental measurements of the TTD-MS RCA. The designed TTD-MS RCA achieves a peak gain of 17.5 dBi and features a 3dB bandwidth of 21.3%, from 11.95 GHz to 14.80 GHz, which closely matches that of the RCA with the SMG. The cavity height is also reduced by 20% with the addition of the TTD-MS. The successful planarization of this broadband RCA should inspire new directions for using metasurfaces for RCA construction.

## II. RCAS WITH SPHERICAL AND DISCRETIZED GROUNDS

### A. RCA WITH THE SPHERICALLY MODIFIED GROUND

Fig. 1(b) shows the configuration of the RCA with a SMG, which was first proposed in [14]. The SMG has a planar circular surface at the center, which gets spherically modified moving toward the edge of the ground. The PRS and the SMG have a circular geometry with the same footprint ( $r_2 = 2.24\lambda_0$  at 12 GHz). It is demonstrated that utilizing such a SMG as a ground plane of the conventional RCA excites higher-order cavity modes and improves the GBP. The resonance frequency of the higher order modes,

**TABLE 1.** Design parameters for the discretized modified ground and true-time-delay metasurface.

Parameter	Value (mm)	Parameter	Value (mm)
$h_1$	0.8	$d_1$	10.2
$h_2$	1.165	$d_2$	9.4
$h_3$	1.355	$d_3$	8.235
$h_4$	1.50	$d_4$	6.88
$w$	8	$d_5$	5.38

$HE_{\ell+1,p+1}$  with  $\ell$  and  $p$  as azimuthal and radial mode numbers respectively, can be approximately determined by the following expression [14]:

$$f_{HE} = \frac{c}{2h_c} \left[ q + 1 + \left( \frac{2p + \ell + 1}{\pi} \right) \cos^{-1} \sqrt{\left( 1 - \frac{h_c}{R_3} \right)} \right] \quad (2)$$

where  $q$  is the axial mode number ( $q = 1$ ), and  $R_3$  is the radius of curvature of the spherical ground. With the theoretical investigation of (2) and the directivity simulations of RCA for different cavity orders, [14] concludes that the resonant frequencies of the modes are more spread out in frequency for the first-order cavity than the second-order cavity. Therefore, it is concluded that the RCA, when designed using the SMG with second-order resonance (where the cavity height is  $1\lambda_0$ ), exhibits a broader 3dB-gain bandwidth compared to the fundamental or third-order resonance configurations (where the cavity height is  $0.5\lambda_0$  and  $1.5\lambda_0$ , respectively) [14] (Fig. 2). Therefore, a cavity height of one wavelength ( $1\lambda_0$ ) is utilized in the design of the RCA with SMG. In the following, a discretized ground is designed to replace the SMG.

### B. RCA WITH THE DISCRETIZED MODIFIED GROUND

Fig. 1(c) depicts a lateral perspective of the RCA with DMG. It has been shown in [42], [44] that the SMG can be replaced by a DMG of 5 levels without an appreciable degradation to the performance of the RCA. We hence discretize the SMG into 5 levels. Mindful that we will eventually replace the DMG with metasurface unit cells, we attempt to discretize the radius into annular rings of width  $w$ , where  $w$  ranges from  $\lambda_0/2$  to  $\lambda_0/4$ . We have observed in previous works [46], [47] that this size allows one to design a wide range of inductive and capacitive components while the composite surface maintains the salient properties of the metasurface, such as wide-angle operation. The inner-most disk of radius  $3w$  is implemented by a planar metallic disk at distance  $h_c$  from the PRS; four rings, each of width  $w$ , are implemented by planar, annular conductive surfaces at heights  $h_1$  to  $h_4$  from the inner-most disk, as labeled in Fig. 1(c). Fine-tuning the DMG RCA using the full-wave electromagnetic simulator Ansys HFSS leads to the optimized DMG parameters shown in Table 1. Fig. 2 compares the realized gains of the RCA with an SMG, a DMG, and flat ground, and shows that the RCA with the DMG indeed has a gain and bandwidth approaching the one with the SMG, while both achieve bandwidths that are much higher than the RCA with the flat

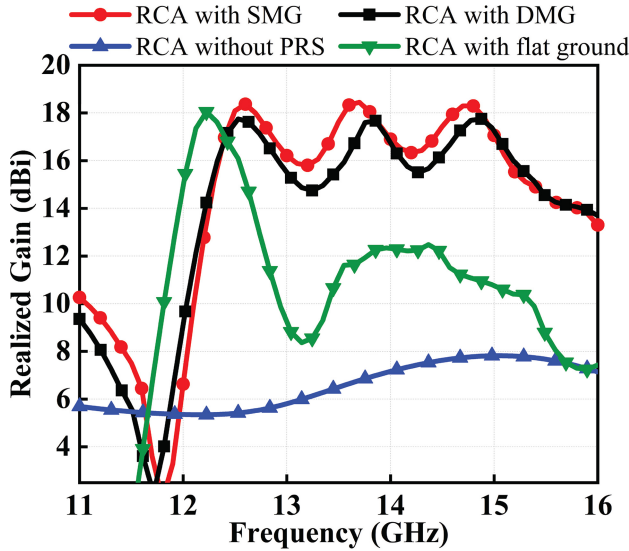


FIGURE 2. Realized gains comparison of the RCA with different cavity configurations.

ground. Converting the RCA's SMG into a DMG prepares us for implementation with a single planar TTD-MS.

### III. RCA WITH THE TRUE-TIME-DELAY METASURFACE

#### A. PROBLEM FORMULATION

We consider a TTD-MS, placed inside the cavity at a new height  $h_{c,new}$  as shown in Figs. 1(c-d). The location of such a surface is marked in a red dashed line in Fig. 1(c). The height  $h_{c,new}$  is properly chosen such that (i) it is sufficiently large to allow an incident wave from the waveguide to couple into the cavity, hence with negligible return loss, (ii) the resultant TTD-MS possesses a range of delays which is reasonable for implementation, and (ideally) (iii) the vertical profile of the antenna is somewhat reduced compared to the SMG and DMG RCAs. The considered surface has a planar geometry and is discretized into sub-wavelength unit cells which are capable of producing the necessary time delays on its surface to compensate for extra distances the electromagnetic waves propagate in the presence of the DMG. For example, as shown in Fig. 1(c), the TTD-MS needs to achieve similar electromagnetic responses at five different regions to mimic the DMG for which the waves travel extra distances ( $d_n$  where  $n = 1$  to 5) and reflect from the annular PEC grounds. The successful implementation of TTD-MS inside the cavity provides a planarized solution that not only eliminates the need for having an SMG or DMG but also reduces the height of the RCA and greatly simplifies its construction. It is hence an attractive route to construct a high-gain, broadband, and low-profile RCA.

TTD-MS design is accomplished through the following procedure:

1) Choose the compensation distances  $d_n = h_c - h_{c,new}$  for each level, which the TTD-MS unit cells will need to implement. In this regard, the analysis in Section II-B is helpful to implement the DMG.

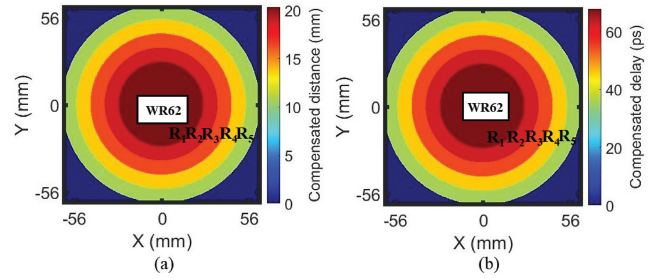


FIGURE 3. The performance required by the metasurface at  $h_{c,new}$ . (a) Distance compensation profile. (b) Delay compensation profile.

2) Calculate the time delays based on the chosen distances  $d_n$  as

$$\tau_{g,n} = \frac{\partial \phi_n}{\partial \omega} = \frac{-2d_n}{c} \quad n = 1, 2, \dots, 5 \quad (3)$$

3) Calculate the needed broadband reflection phase response as

$$\phi_n(\omega) = \omega \tau_{g,n} + \pi \quad n = 1, 2, \dots, 5 \quad (4)$$

4) Design metasurface unit cells with the broadband reflection phase response.

5) Piece together the metasurface unit cells to form the TTD-MS.

In the above equations  $2d$  represents the round trip distance, the waves travel in the case of the DMG compared with TTD-MS, and  $\pi$  represents the reflection from the PEC ground. Note that the required reflection phases vary linearly with frequency, demanding a special kind of surface, a TTD-MS, to be built where phase dispersion is minimum. We emphasize that the proposed unit cells that populate the TTD-MS should mimic the DMG in the aspects of both time delay and phase progression. This means that (3) and (4) must be satisfied simultaneously. This marks a departure from most previous TTD-MSs, for which only the proper delay needs to be achieved along with a relative phase relationship among elements at the design frequency. We plot the required compensation distances and time delays required by the TTD-MS in Figs. 3(a) and 3(b) respectively. The sub-figures show the top view of the surface (in  $-z$ -direction) inside the cavity where regions  $R_n$  (where  $n = 1$  to 5) represent five concentric rings. The maximum and minimum compensation distances are 20.3 mm and 10.7 mm, at the center and the outer edge of the surface, respectively, and the maximum and minimum time delays are 68 ps and 35.6 ps within these regions. As expected, and as observed from (3) and (4), the TTD-MS is radially symmetric as it replaces a radially symmetric DMG.

#### B. THEORETICAL FORMULATION

In this section, we report the design procedure for the TTD-MS. To better understand the functionality of the TTD-MS, we consider a generic metasurface, as shown in Fig. 4(a). The metasurface consists of an array of sub-wavelength unit cells that collectively make up its aperture.

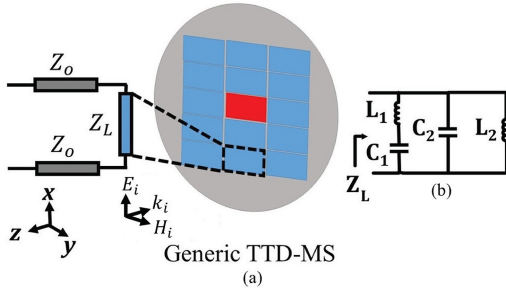


**FIGURE 4.** (a) A generic representation of the TTD-MS. (b) The equivalent circuit diagram of a fourth-order Bessel filter implemented by the TTD-MS unit cell.

This particular view in Fig. 4(a) depicts the situation when the waves incident on the TTD-MS after getting reflected from the PRS. The incident electric field, magnetic field, and wave vectors are represented as  $\mathbf{E}_i$ ,  $\mathbf{H}_i$  and  $\mathbf{k}_i$  which are in the  $x$ ,  $y$ , and  $-z$  direction respectively. We consider a normal incidence situation with an  $x$ -directed electric field. This incidence can be represented by the equivalent circuit in the inset of Fig. 4(a), where  $Z_0 = 377\Omega$  is the incident wave impedance of the impinging wave and  $Z_L(\omega)$  is the frequency-dependent load impedance that we seek to implement with a metasurface. The desired time delay ( $\tau_{g,n}$  or  $\frac{\partial\phi_n(\omega)}{\partial\omega}$ ) we wish to achieve is related to the load impedance through the reflection coefficient:

$$\Gamma(\omega) = \frac{Z_L(\omega) - Z_0}{Z_L(\omega) + Z_0} = -e^{-j\phi_n(\omega)} \quad (5)$$

We assume that the load is purely reactive. A metasurface composed of unit cells with the frequency-dependent load impedance, or equivalently, the frequency-dependent reflection response in (5) will cause the same group delay profile as the DMG in the previous section at  $h_{c,new}$ , and hence planarize the RCA design. We implement the low pass LC network shown in Fig. 4(b) to realize the frequency-dependent load impedance in  $\Gamma(\omega)$  over the desired operating frequency. The circuit has two inductors and two capacitors that provide a series LC and a parallel LC resonance tank, arranged in a parallel configuration. We find that this circuit is relatively simple to implement due to the fact that the elements are co-located in a shunt configuration. Written in the Laplace space, the frequency-dependent input impedance of such a circuit can be given as:

$$\begin{aligned} Z_L(s) &= \frac{P_M(s)}{Q_N(s)} \\ &= \frac{s^3 L_1 L_2 C_1 + s L_2}{s^4 L_1 C_1 L_2 C_2 + s^2 L_1 C_1 + s^2 L_2 C_2 + s^2 L_2 C_1 + 1} \end{aligned} \quad (6)$$

Substituting (6) into (5) yields

$$\Gamma'(s) = \frac{P_M(s) - Z_0 Q_N(s)}{P_M(s) + Z_0 Q_N(s)} = \frac{P_{\Gamma'}(s)}{Q_{\Gamma'}(s)} = -e^{-j\phi_n(\omega)} \quad (7)$$

where  $s = j\omega$  represents the frequency axis on the Laplace plane. The zeros and poles of  $\Gamma'(s)$  are located at mirrored

locations about the  $j\omega$  axis, thus they contribute equally to cause the desired group delay  $\frac{\partial\phi_n(\omega)}{\partial\omega}$  in  $\Gamma'(s)$  while keeping  $|\Gamma'(s)| = 1 \forall \omega$ . To simplify the formulation, we match the denominator of  $\Gamma'(s)$  to a desired  $Q_{\Gamma'}(s)$  which achieves half of the desired group delay in  $\Gamma'(s)$ , knowing that the corresponding  $P_{\Gamma'}(s)$  will provide the other half of the desired group delay.

In filter design theory, it is well known that the Bessel filter can provide a phase that varies linearly with frequency – hence resulting in a constant time delay – over a broad bandwidth [48]. Recent works have employed this property to construct TTD-MSs [47], [48], [49], [50], [51], [52], [53]. We design our TTD-MS following the formulation of [47] where an ultra-wideband reflect-array, producing relative time delays on its aperture, is designed with the TTD concept. Whereas the application [47] requires only the achievement of relative reflection phases and group delays among the metasurface elements, our usage of the TTD-MS within a cavity requires us to achieve the absolute reflection phase and group delay with each TTD-MS element. To our knowledge, this is the first application of a TTD-MS within a cavity environment.

In this work, we achieve constant time delay for our metasurface unit cells by implementing a 4th order Bessel filter for  $Q_{\Gamma'}(s)$  using the topology shown in Fig. 4(b). We find that this filter order is relatively simple to implement yet sufficient to provide the needed maximum time delay over our desired frequency band. A potential improvement in bandwidth and the range of delay is possible with a higher-order filter, at the cost of a more complicated unit cell design. We realize the desired  $\Gamma'(s)$  by the following process: 1) Set the coefficients of  $Q_{\Gamma'}(s)$  for each metasurface unit cell to the 4<sup>th</sup> order Bessel filter polynomial. 2) Extract the component values  $L_1$ ,  $C_1$ ,  $L_2$  and  $C_2$  as a function of group delay and wave impedance. 3) Design a metasurface unit cell that achieves the desired component values as found in Step 2. We expand the denominator of (7) to write:

$$\begin{aligned} Q_{\Gamma'}(s) &= s^4 L_1 C_1 L_2 C_2 + \frac{1}{Z_0} s^3 L_1 L_2 C_1 + s^2 \\ &= (L_1 C_1 + L_2 C_2 + L_2 C_1) + \frac{1}{Z_0} s L_2 + 1 \end{aligned} \quad (8)$$

We compare this with the Laplace space expression for the denominator of the fourth-order Bessel filter with a delay of  $\tau_f$  at DC:

$$\frac{1}{105(\tau_f s)^4} + \frac{10}{105(\tau_f s)^3} + \frac{45}{105(\tau_f s)^2} + \tau_f s + 1 \quad (9)$$

We equate (8) and (9), and simplify to get the expression of components as a function of group delay and wave impedance:

$$L_1 = 0.41\tau_f Z_0; \quad L_2 = 1.00\tau_f Z_0 \quad (10)$$

$$C_1 = \frac{0.23\tau_f}{Z_0}; \quad C_2 = \frac{0.10\tau_f}{Z_0} \quad (11)$$

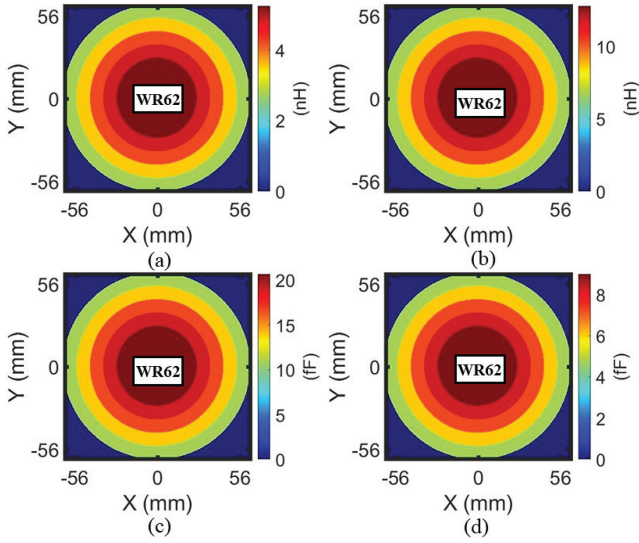


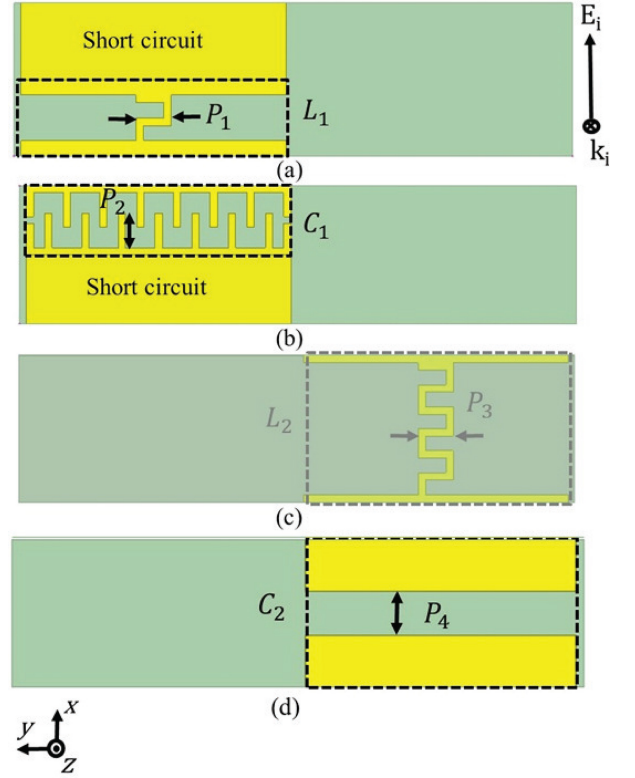
**FIGURE 5.** Required component values corresponding to the group delay of  $\Gamma'(s)$ . (a)  $L_1$  (b)  $C_1$  (c)  $L_2$  (d)  $C_2$ .

We set  $\tau_f = \frac{\tau_g}{2}$  and use (10) and (11) to find the lumped elements which produce the desired group delays. Following this methodology, we calculated the desired component values for all the required delays in (3) as shown in Fig. 5.

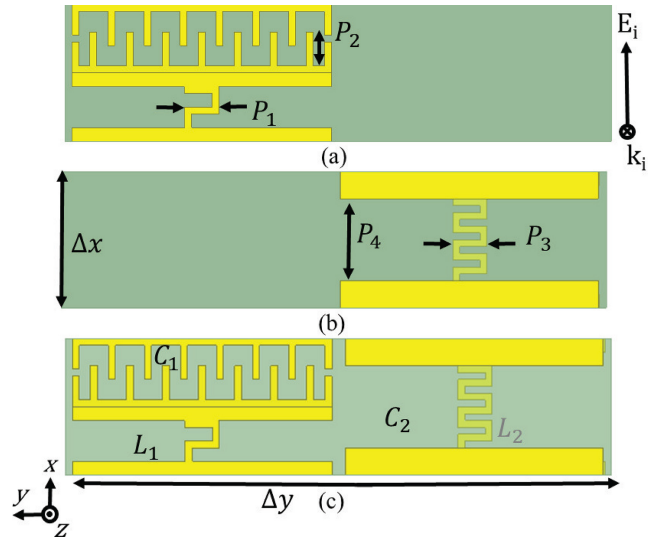
### C. UNIT CELL DESIGN

We now design the unit cells with the required reflection phases  $\frac{\partial \phi_n(\omega)}{\partial \omega}$  and time delays  $\tau_{g,n}$  in  $\Gamma'(s)$  for different regions over the TTD-MS aperture. Many recent works have used printed circuit boards to implement metasurfaces from microwave to mm-wave frequencies [53], [54], [55], [56], [57], [58], [59], [60], [61]. However, the physical realization of the lowpass LC network in Fig. 4(b) requires the presence of four circuit elements ( $L_1$ ,  $C_1$ ,  $L_2$ ,  $C_2$ ) on the same plane, without separation by a PCB of appreciable thickness. The close spacing of resonant elements means it is important to properly account for their interactions in the design process. Moreover, whereas previous TTD-MSs [46], [47], [50], [51], [52] mostly emphasize on generating the required time delays, in our case, the TTD-MS needs to generate both the correct reflection phase and the required time-delay. This places an unprecedented requirement on the property of the achieved cell.

We realize the metasurface using the printed circuit topology as shown in Figs. 6-7. We first develop and study each component separately, as shown in Fig. 6. This step is essential in investigating the capability of each element to realize the required reactances. With the library of data from Fig. 6, we proceed to develop the actual TTD-MS unit cell shown in Fig. 7. Fig. 7(c) shows our printed TTD-MS unit cell, which implements the Bessel filter of Fig. 4(b). We use the Rogers RT/duroid 5880 board ( $\epsilon_r = 2.2$ ,  $\tan \delta = 0.0012$ ) with 0.127 mm thickness ( $0.00508 \lambda_0$  at 12 GHz) as dielectric support for the printed components. The dimensions of the unit cell are 8 mm  $\times$  2 mm. Yellow



**FIGURE 6.** Printed circuit components for a lumped circuit of Fig. 4(b): (a) Printed inductor  $L_1$  with a short circuit. (b) Printed capacitor  $C_1$  with a short circuit. (c) Printed inductor  $L_2$  on the backside of the PCB board. (d) Printed capacitor  $C_2$ .

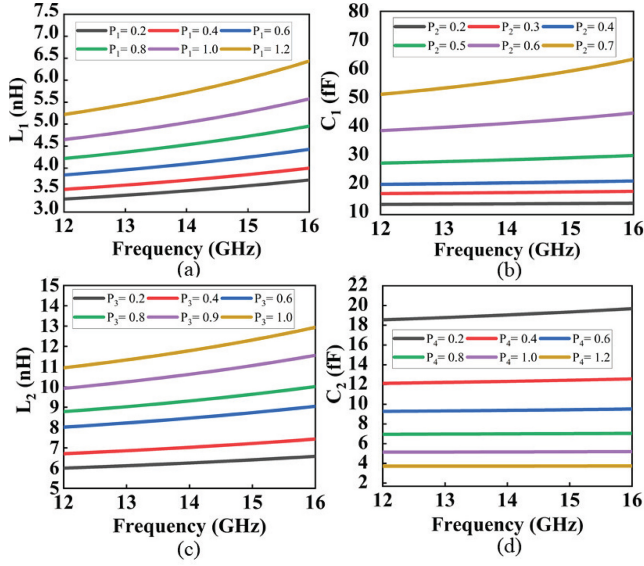


**FIGURE 7.** The TTD-MS unit cell with metallic patterns depicted (yellow). (a) Series half circuit. (b) Parallel half circuit. (c) Full circuit.

represents etched metallic patterns on the dielectric slab where a series  $L_1 C_1$  with a parallel  $C_2$  resides on one side of the dielectric slab and a parallel  $L_2$  is etched on the other side. We construct  $C_1$  with the interdigitated capacitor,  $C_2$  with the gap capacitor, and  $L_1$  and  $L_2$  with the meander lines.

TABLE 2. Simulated ranges for the geometric parameters defined in Fig. 6.

Unit cell confi.	Parameter	Range (mm)	Step (mm)
Fig. 6(a)	$P_1$	[0, 1.2]	0.05 linear
Fig. 6(b)	$P_2$	[0, 0.7]	0.025 linear
Fig. 6(c)	$P_3$	[0, 1]	0.05 linear
Fig. 6(d)	$P_4$	[0, 1.2]	0.025 linear

FIGURE 8. Extracted  $L_1$ ,  $C_1$ ,  $L_2$ ,  $C_2$  from the printed circuits by varying geometric parameters  $P_1, P_2, P_3, P_4$  units (mm). (a)  $L_1$ . (b)  $L_2$ . (c)  $C_1$ . (d)  $C_2$ .

In the following, we describe our procedure to design the TTD-MS unit cells that achieve the required circuit parameters and provide a constant time delay over the working bandwidth.

We follow three steps process to realize our TTD-MS unit cell. We start by designing each printed component separately, as shown in Fig. 6. We surround each component with periodic boundaries (in x- and y-directions) and apply Floquet port excitations to simulate wave incidence in the -z-direction. We define four geometrical parameters – ( $P_1$ ,  $P_2$ ,  $P_3$ , and  $P_4$ ) as shown in Fig. 6 – that we sweep within a predefined range as given in Table 2. Changing  $P_1$ ,  $P_2$ ,  $P_3$ , and  $P_4$  will change  $L_1$ ,  $C_1$ ,  $L_2$  and  $C_2$  respectively. The electromagnetic simulation yields reflection and transmission coefficients ( $S_{11}$  and  $S_{21}$ ), from which the impedance can be found through [61] as:

$$Z(\omega) = \frac{Z_o}{2} \frac{1 + S_{11} + S_{21}}{1 - S_{11} - S_{21}}; \quad (12)$$

where  $Z_o$  is the intrinsic impedance of free space. Finally, the reactive components can be found via  $Im(Z) = j\omega L_n$  or  $Im(Z) = -j/\omega C_n$ , where  $n = 1$  or  $2$ . The procedure of extracting reactance values from a periodic simulation is well documented in previous works, for example, in [56]. Fig. 8 plots the extracted  $L_1$ ,  $C_1$ ,  $L_2$  and  $C_2$  against the geometric parameters  $P_1$ ,  $P_2$ ,  $P_3$ ,  $P_4$ . As can be expected, increasing meander line lengths  $P_1$  and  $P_3$  produce increased

TABLE 3. Geometric parameters of the proposed TTD-MS.

Regions	$P_1$ (mm)	$P_2$ (mm)	$P_3$ (mm)	$P_4$ (mm)
$R_1$	0.7	0.525	1.55	0.5
$R_2$	0.6	0.475	1.3	0.6
$R_3$	0.6	0.4	0.8	0.8
$R_4$	0.45	0.3	1.2	0.8

inductances  $L_1$  and  $L_2$  respectively. Likewise, increasing the interdigitated finger length  $P_2$  and reducing the gap distance  $P_4$  correspondingly increase the capacitances  $C_1$  and  $C_2$ . Note that (10)-(11) show the required  $L_1$ ,  $L_2$  and  $C_1$ ,  $C_2$  should be invariant. However, the simulated circuit elements change with frequency. This variation becomes severe for higher component values. The capacitors are almost constant for the range of values required to build our TTD-MS (Fig. 5), though the inductors show a variation of 1 nH over the frequency range. Considering this, we match the intended inductors with the simulated inductors at the center frequency. We believe this consideration would not significantly affect the bandwidth of the TTD-MS. This stage of simulation allows us to correlate the geometric parameters of the metasurface to the reactive component values and readies us for their combination in the following steps.

Next, we combine the elements together in the process to achieve the metasurface unit cell. We first combine  $L_1$  and  $C_1$ , and  $L_2$  and  $C_2$ , to achieve two metasurface semi-cells, as shown in Figs. 7(a-b). Finally, we combine the two semi-cells to form the full unit cell in Fig. 7(c). We obtain the simulated reflection and transmission coefficients in both stages and find  $Z(\omega)$  through (12). As intra-cell mutual coupling effects will slightly modify the effective values of the circuit components, we fine-tune the geometric parameters ( $P_1$  to  $P_4$ ) in both steps to ensure the simulated reactances  $Im(Z)$  agree with the required values found from the previous section. Finally, we implement the termination of the metasurface. The equivalent circuit of Fig. 4(b) is left open-circuited (after  $L_2$ ). In metasurface design, this is equivalent to placing a perfect magnetic conductor (or infinite impedance surface) behind the reactive components. In this work, we realize this by placing a flat metallic ground at a quarter-wavelength (at the center frequency) away from the printed components. This completes the metasurface unit cell design.

Accurately tuned reactances of the full circuit generate the required reflection coefficients according to (5). Table 3 lists the required physical dimensions of the unit cells to design the required TTD-MS. Fig. 9(a) compares the designed reflection phase of printed unit cells ( $|\angle \Gamma'(s)| = \frac{\partial \phi_n(\omega)}{\partial \omega}$ ) against the required reflection phase calculated from (4), at different regions on metasurface. It can be seen that the designed unit cells maintain linear phase variations over a broad bandwidth and well approximate the required reflection responses: this validates the true-time-delay nature of our designed TTD-MS unit cells. A maximum deviation of  $|\angle S_{11,designed} - \angle S_{11,ideal}| < 20^\circ$  is present between

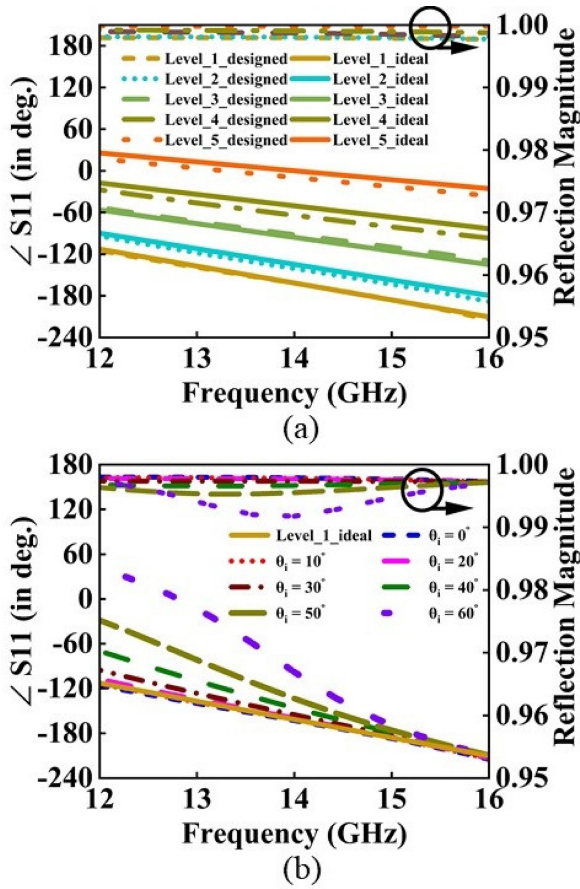


**FIGURE 9.** Study on the reflection properties of the TTD-MS unit cells. (a) Comparison of the simulated reflection coefficients of the designed TTD-MS unit cells with the ideally required reflection coefficients calculated by (3). (b) The effect of oblique incidences on the TTD-MS unit cell performance.

the ideally required and the achieved phases over the entire operation band of interest, ranging from 12 GHz to 16 GHz. Also, all the unit cells have a reflection magnitude of more than 0.99 over the entire operation bandwidth.

Considering that in our TTD-MS RCA, the distance between the PRS and the metasurface is small, we investigated the effect of oblique wave incidences on the unit cell performance. To illustrate our analysis, Fig. 9(b) shows the Region 1 unit cell's reflection phase's variation under different incidence angles. We compare the simulated reflection phases with the ideally required phase to observe the angular stability of the unit cell. Up to the oblique incidence of  $30^\circ$ , we can see that the simulated reflection phases closely match the ideally required phase with the intended slope. Therefore, the proposed unit cell provides angle-insensitive operation for the small angles. Beyond this angle, at the lower band, the phase deviates sharply from the ideal phase curve, which also affects the curve's slope. Nonetheless, the reflection magnitude remains over 0.99 in the entire operation bandwidth. Further, we place the designed unit cells at their respective regions within the RCA to obtain the full metasurface structure.

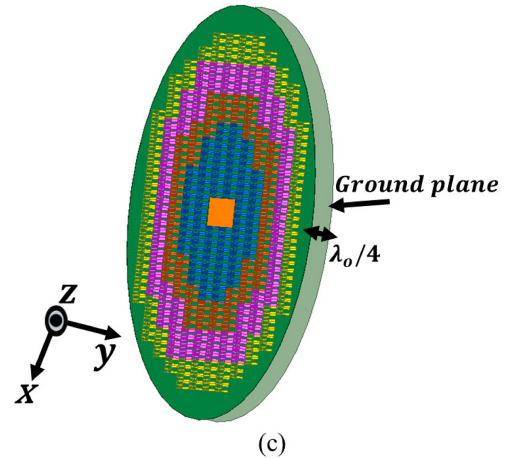


**FIGURE 10.** A diagram of the proposed TTD-MS. (a) Top view of the TTD-MS. (b) Bottom view of the TTD-MS. (c) A perspective view of the proposed TTD-MS with the backing of a PEC plate.

Figs. 10(a-b) show the top and bottom views of the metasurface. Metallic traces for components  $L_1$ ,  $C_1$  and  $C_2$  are placed above the substrate while the component  $L_2$  is placed below the substrate. Different colors indicate the different regions  $R_n$  with different time delays. Each region has its own set of unit cells arranged in an approximately rotationally symmetric fashion. The required time delay in  $R_5$ , located in the outer region of the metasurface, can be achieved without the metallic patterns. We place the

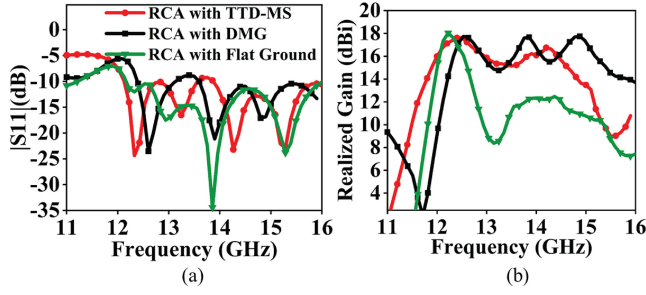


**FIGURE 11.** Comparison of the simulated  $S_{11}$  and realized gain of the RCA with different antenna configurations: the discretized modified ground, the true time delay metasurface, and the metallic ground. (a)  $S_{11}$ . (b) Realized gain.

TTD-MS with the backing of a metallic ground plan at  $h_{c,new}$  location inside the cavity to construct the TTD-MS RCA. Fig. 10 (c) shows a side view of the proposed TTD-MS.

#### IV. RCA WITH TTD-MS: SIMULATION RESULTS

This section reports simulation results comparing our TTD-MS RCA to RCAs with a DMG and flat ground. All RCAs are fed by WR-62 waveguides, and Rogers 6010 substrate with a dielectric constant of 10.2 and a thickness of 1.90 mm is used as their PRSs. All PRSs and ground planes are circular with a common radius of 56 mm ( $2.24\lambda_0$  at 12 GHz). The cavity heights in the cases of DMG and flat ground are  $1\lambda_0$ ; the TTD-MS slightly reduces this height to  $0.80\lambda_0$ . We use Ansys HFSS to simulate our models.

Fig. 11 compares the simulated reflection coefficient ( $S_{11}$ ) and the realized gain of the RCA designs. From the  $S_{11}$  plot, one can see that all antenna designs radiate efficiently within the bandwidth from 12 GHz - 16 GHz. Notably, the TTD-MS RCA achieves adequate broadband impedance matching despite having a reduced cavity height. From the plot for the realized gain, we see that the TTD-MS RCA achieves a 21.7% 3dB-gain bandwidth (from 11.9 GHz - 14.8 GHz). This 3dB-gain bandwidth approaches that of the DMG RCA (23%) and is much improved over the flattened ground RCA (5%). However, the gain curve of the TTD-MS RCA is slightly shifted towards the lower frequency as compared to the DMG RCA. This shift is approximately 0.5 GHz. This shift forces the TTD-MS RCA to have a lower gain than the DMG RCA from 15 GHz-16 GHz and a better gain from 11.5 GHz-12.5 GHz. Within the working band, the TTD-MS RCA achieves a maximum realized gain of 17.6 dBi (at 12.2 GHz), which closely approaches the DMG RCA (17.9 dBi) and the flat ground RCA (17.95 dBi). The GBP for the DMG RCA and the TTD-MS RCA are 14.2 and 12.5, respectively. The TTD-MS RCA realizes a peak aperture efficiency of 28%, which is comparable to that of the DMG RCA (30%). We have hence successfully flattened the ground plane of the RCA with a minimal sacrifice in the antenna performance.

Fig. 12 shows the E-plane and H-plane radiation patterns of the DMG RCA and the TTD-MS RCA at three different frequencies of 12.5 GHz, 13.1 GHz, and 14.1 GHz. A

comparison of these radiation patterns with [14, Fig. 8] shows that these patterns correspond well to the SMG RCA. Specifically, the radiation patterns shown in Fig. 12 and the 2D field profiles within the cavity show that at the above three frequencies, the  $HE_{11}$ ,  $HE_{12}$ , and  $HE_{13}$ , modes are the respective dominant radiating modes. It can be seen that the TTD-MS RCAs approximate the DMG RCA at all three frequencies, apart from a slight reduction of the H-plane sidelobes near the second mode and a slight increase of the E-plane sidelobes of the third mode. We observe that the radiation pattern contains a clear main lobe in all cases.

Sidelobe levels are below -10 dB for near the fundamental mode, but appreciable sidelobes (reaching -6dB) emerge on the E-plane for the higher-order modes for both the TTD-MS RCA and DMG RCA. We note that similar SLLs are also observed from [14], hence our metasurface has mimicked the SMG and brought along its advantages and disadvantages. Our simulations show the effectiveness of the TTD-MS again in mimicking and planarizing the DMG. The cross-polarization of the antenna in the E and H plane for three different frequencies – (a) 12.5 GHz (b) 13.1 GHz. (c) 14.1 GHz – are shown in Fig. 13. The cross-polarization of the proposed antenna is below -22 dB at the broadside direction over the working band. We further plot the sidelobe level (SLL) of the proposed antenna across the working band (from 11.8 GHz - 15 GHz) in Fig. 14. It is shown that the proposed antenna has a maximum and minimum SLL of 16 dB and 5.5 dB at 12.2 GHz and 13.7 GHz respectively. These higher sidelobes of waves emanating from an RCA often result from phase non-uniformity across the aperture, and in these cases, the inclusion of an appropriate phase-correcting surface (PCS) that removes the phase non-uniformity will appreciably increase the gain and decrease the sidelobe level. Further study with placing a TTD-MS metasurface, functioning as PCS, atop the PRS (or replacing the PRS) could resolve such sidelobe issues and further improve the radiation pattern of the RCA.

#### V. EXPERIMENTAL VALIDATION

##### A. MEASUREMENT RESULTS

Fig. 15(a) shows the fabricated RCA; the PRS moved to one side to reveal the TTD-MS. The standard PCB etching technology is used to fabricate the TTD-MS. The supporting structures holding the TTD-MS, PRS, and connections to the waveguide were produced with a 3D printer. Styrofoam with a thickness of 5 mm is used as a spacer layer between the TTD-MS and a ground plane. A WR-62 waveguide feeds the TTD-MS RCA. The  $S_{11}$  and gain performance are measured using a Keysight N5260A vector network analyzer and Satimo StarLab Near-field Antenna Measurement System, respectively.

Figs. 15(b) and 15(c) compare the measured and simulated  $S_{11}$  and gain performances of the proposed RCA. As seen in Fig. 15(b), the measured and simulated  $S_{11}$  agrees well with one another; a measured bandwidth (for  $S_{11} < -10dB$ ) of 32% is achieved, spanning from 12-16.5 GHz. The slight

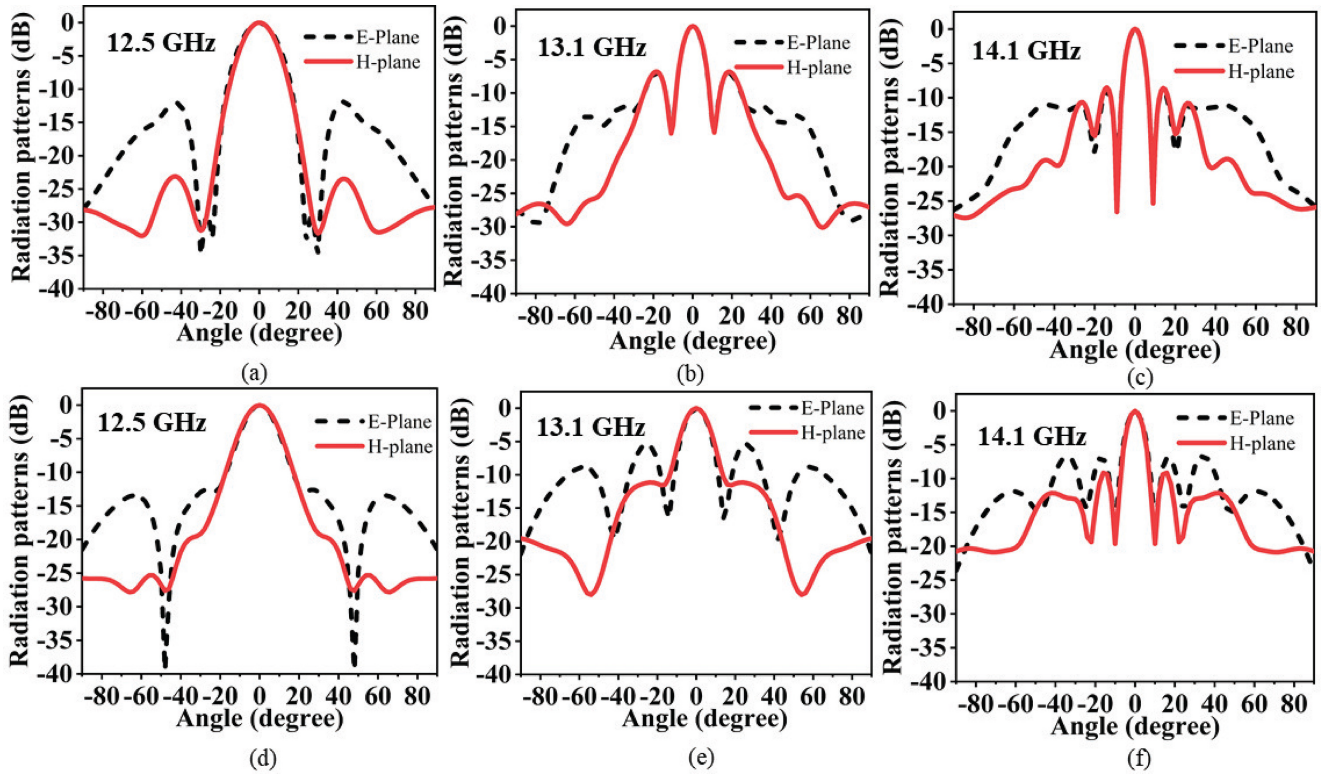


FIGURE 12. Simulated normalized radiation patterns of the DMG RCA (top row) and the TTD-MS RCA (bottom row).

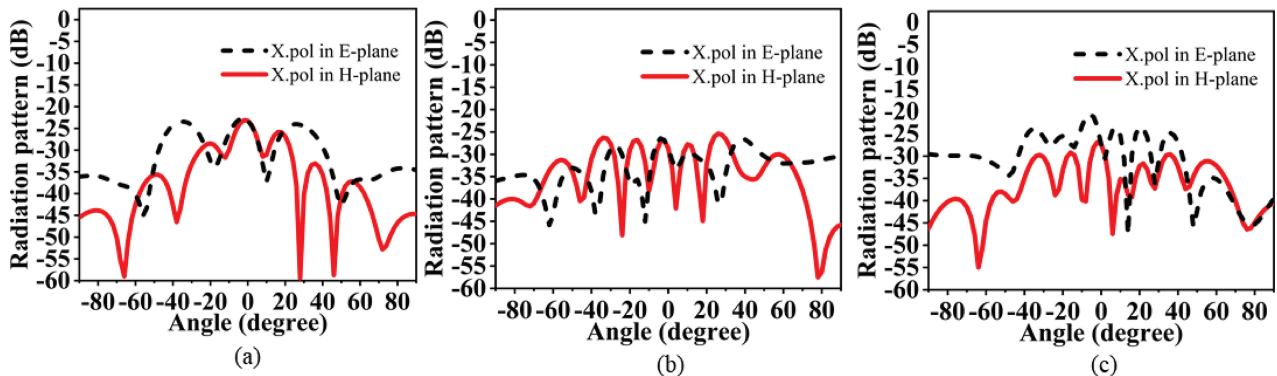


FIGURE 13. Cross polarization of the proposed antenna. (a) 12.5 GHz. (b) 13.1 GHz. (c) 14.1 GHz.

discrepancies between simulated and measured results are most likely due to the fabrication tolerances. Fig. 15(c) also shows a good agreement between the measured and simulated realized gains. The measured 3-dB gain bandwidth is 21.3%, ranging from 11.95 GHz to 14.8 GHz; we find the peak gain slightly drops to 17.5 dB from the simulated value of 17.6 dB, thus settling the measured GBP to 12. Compared with the RCA with flat ground, the 3dB-gain bandwidth is enhanced from 5% to 21.3%. The simulated and measured radiation patterns, both in E and H planes, at three different frequencies, are shown in Fig. 16. It is observed that the simulated and measured radiation patterns are in agreement and that directive radiation is achieved with sidelobes below  $-10$  dB at 12.5 GHz. Due to the characteristic of the

higher-order cavity modes, the sidelobe is slightly higher at 13.1 GHz and 14.1 GHz, as also observed with the spherical ground plane in [14].

## B. DISCUSSION

In this section we make remarks about the achievement of the TTD-MS RCA demonstrated in this paper, its relations to previous works, and its potential for extensions.

In this work, we demonstrated how the TTD-MS can enact QLG modes inside the cavity to broaden the RCA gain bandwidth. The designed antenna achieves a peak gain and 3dB bandwidths similar to the SMG RCA it seeks to replace. The form factor has been planarized, leading to straightforward fabrication. The height is also further reduced

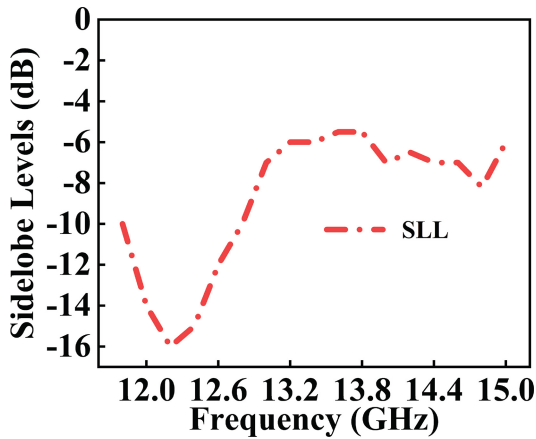


FIGURE 14. Sidelobe levels of the proposed antenna.

by 20%. The thin form factor will be attractive for system-level integration.

We discuss our contribution from the perspective of metasurface design and deployment. While the many metasurfaces [53], [59], [61] engineer the surface impedances at a single frequency to achieve different functionalities, we engineer the impedances of the unit cells to generate a linear reflection phase in a broadband operation. This class of metasurface is called the TTD-MS because its broadband response matches that of a true-time-delay network. Moreover, whereas previous TTD-MSs are designed to introduce a required group delay to a wave that only interacts with the surface once, in our work, the metasurface is designed to work within a cavity environment, where the cavity modes interact with the metasurface many times and multiple incident reflected waves superimpose together. This places an unprecedented requirement on both the reflection phase and the group delay of the metasurface unit cells. In this perspective, the successful achievement of the TTD-MS RCA represents an advancement in the deployment of the TTD-MS toward the design of the metasurface-enabled antennas.

Table 4 compares the performance of the proposed antenna with other RCA designs of three different classes: RCAs with smaller apertures [13], [20], RCAs with multilayers PRS [15], [21], [23], [24], [25], [26], RCAs with modified grounds [14], [41], [44], [45]. It is instructive to point out here that the RCAs with smaller electrical areas exhibit broader 3dB gain bandwidths, although their peak gains are limited due to the smaller radiating apertures, as demonstrated in [22] and [62]. Though a higher peak gain with a smaller aperture is possible [39], [63], it requires a mesh of dielectric slabs of different permittivities [13] or different thicknesses [39] in the axial direction of the antenna to form a PRS. This requires precise cutting and joining of dielectric slabs, and the whole process of constructing the PRS requires extra effort and adds complexities to the design process. This may lead to complicated custom fabrication, heavy antenna weight, and high cost. On the other hand,

TABLE 4. Performance comparison of the proposed antenna with other RCA configurations.

Ref.	Techniques used	Electrical area ( $\lambda_c^{2*}$ )	RCA height ( $\lambda_c^*$ )	Peak gain (dBi)	3-dB bandwidth (%)	GBP
[13]	STPG superstrate	2.84	1.01	15.9	54.2	21.1
[20]	Thin slabs	3.22	0.83	15	50.9	16.09
[21]	Stacked cavity	8.41	1.14	17.5	17.9	10.1
[23]	Stacked cavity	5.40	1.35	15	26.8	8.16
[15]	Two-layer FSS	5.76	0.66	14	32.3	8.11
[24]	Two-layer FSS	127.94	0.57	16.2	15.7	6.5
[25]	Two-layer FSS	5.76	0.55	13.8	28	6.71
[26]	Meta-surface	13.55	0.50	16.3	10.9	4.6
[14]	SMG	24.45	1.25	17.7	25	14.7
[41]	Shaped ground	7.56	0.65	16	19.7	7.84
[44]	SMG	14.32	1.10	17.6	12	6.9
[45]	SMG	32.15	1.16	20	11.6	11.6
This work	TTD-MS	19.58	0.98	17.5	21.3	12

\* free space wavelength at the center frequency of the operating band.

the RCAs with larger electrical areas [21], [24], [26] can provide higher peak gains, but their 3dB gain bandwidths are limited due to the non-uniformity of the phase in the aperture field [13]. Also, constructing the PRSs for such antennas with multilayer structures or metasurfaces add up to the manufacturing cost of the antenna. An alternate method for large aperture RCAs, involving only a single layer of the PRS and a SMG [14], [44], [45], provides higher peak gains with broad 3dB bandwidths by exciting higher order cavity modes. However, this method requires precise fabrication tools and techniques for manufacturing the shaped ground planes. To this, our proposed TTD-MS RCA minimizes the manufacturing complexity, provides a planarized solution to SMG of [14] with reduced cavity height, and uses a single-layer PCB to achieve a high peak gain and 3dB bandwidth. Thus, the proposed RCA provides high gain and wide bandwidth with a simple and planar structure.

The proposed TTD-MS RCA works with x-polarized electric fields as it features a metasurface unit cell that only works with x-polarized electric fields. Nonetheless, the point of the work – proving the viability of the TTD-MS to replace a curved reflector within a cavity environment – is clearly demonstrated. In future, we aim to investigate the dual-polarization operation using a dual-polarized TTD-MS

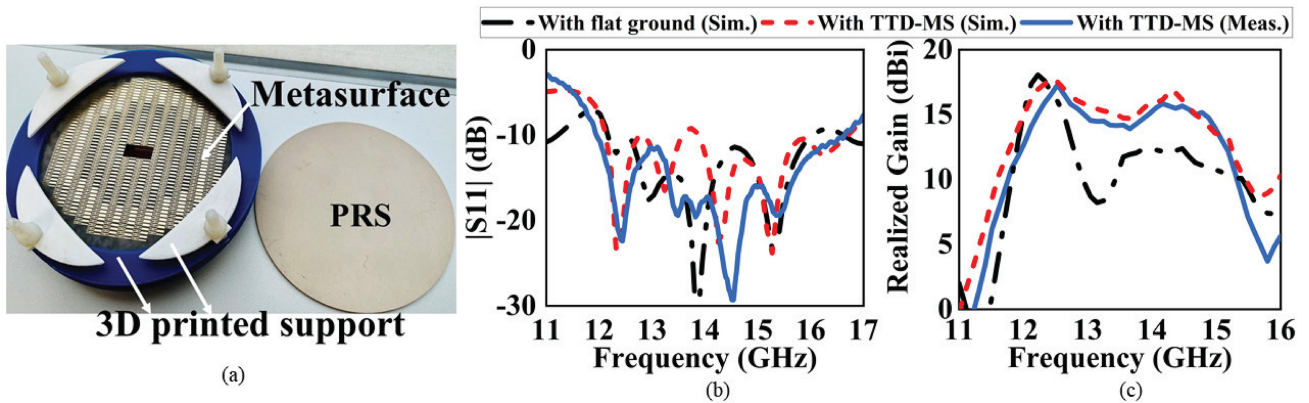


FIGURE 15. Experimental demonstration of the TTD-MS RCA. (a) Fabricated prototype. (b) Reflection coefficient ( $S_{11}$ ). (c) Realized gain.

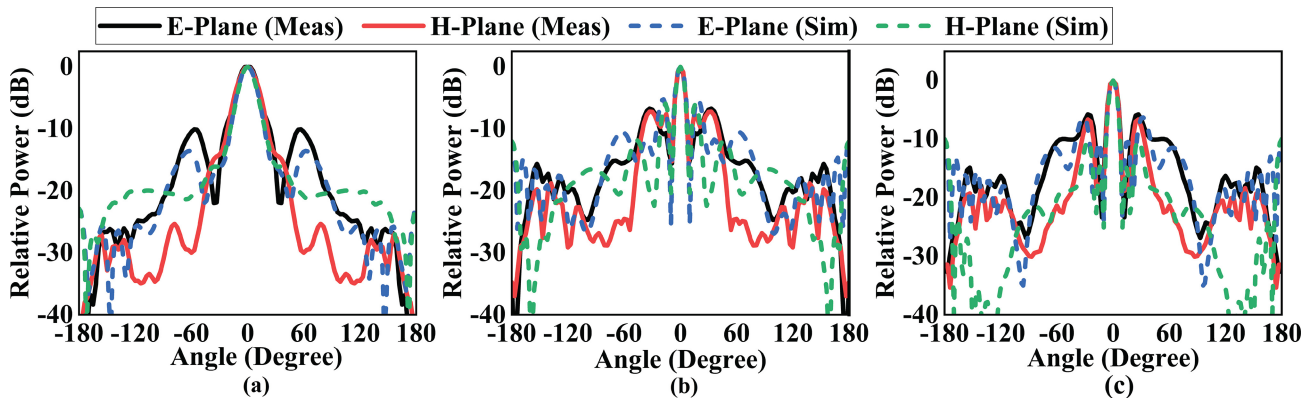


FIGURE 16. Measured and simulated radiation patterns of the proposed RCA at (a) 12.5 GHz. (b) 13.1 GHz. (c) 14.1 GHz.

cell, which possesses xy-symmetry and is hence polarization-insensitive.

## VI. CONCLUSION

In this research, we proposed a novel RCA using an ultrathin true-time-delay metasurface (TTD-MS). We have demonstrated, by simulation and experiment, that the proposed metasurface can approximate a curved spherical ground and pave the way to straightforward fabrication. The TTD-MS RCA provides a similar maximum gain (17.5 dBi) and 3dB-gain bandwidth (21.3%), but dramatically simplifies the fabrication complexities of the SMG RCA. The presented results confirm the effectiveness of the TTD-MS RCA as a high-gain, wideband and compact RCA that lends to simple fabrication. Its planarized design makes it amenable to established PCB fabrication, which can be scaled reliably into the mm-wave range. We expect it will find attractive applications in modern-day communication and imaging systems.

## REFERENCES

- [1] J. Huang and J. A. Encinar, "Introduction to reflectarray antenna," in *Reflectarray Antennas*, 1st ed. Hoboken, NJ, USA: Wiley, 2007, pp. 1–6, ch. 1, Accessed: Apr. 25, 2023. [Online]. Available: <https://books.google.com.hk/books?id=JNwYCzFt8Z0C>.
- [2] L. Guo, Y. Chen, and X. Chen, "A metal-only folded reflectarray antenna," *IEEE Antennas Wireless Propag. Lett.*, vol. 22, pp. 1–5, 2023.
- [3] L. Guo, P.-K. Tan, and T.-H. Chio, "On the use of single-layered subwavelength rectangular patch elements for broadband folded reflectarrays," *IEEE Antennas Wireless Propag. Lett.*, vol. 16, pp. 424–427, 2017.
- [4] Y. Cao, W. Che, W. Yang, C. Fan, and Q. Xue, "Novel wideband polarization rotating metasurface element and its application for wideband folded reflectarray," *IEEE Trans. Antennas Propag.*, vol. 68, no. 3, pp. 2118–2127, Mar. 2020.
- [5] G.-T. Chen, Y.-C. Jiao, G. Zhao, and C.-W. Luo, "Design of wideband high-efficiency circularly polarized folded reflectarray antenna," *IEEE Trans. Antennas Propag.*, vol. 69, no. 10, pp. 6988–6993, Oct. 2021.
- [6] X.-B. Zhao, F. Wei, X. W. Shi, and C. Zeng, "Broadband folded reflectarray antenna using single-layer cross-polarization conversion subwavelength elements," *IEEE Antennas Wireless Propag. Lett.*, vol. 20, no. 4, pp. 612–616, Apr. 2021.
- [7] J. Yang, Q. Cheng, M. K. T. Al-Nuaimi, A. Kishk, and A.-E. Mahmoud, "Broadband folded reflectarray fed by a dielectric resonator antenna," *IEEE Antennas Wireless Propag. Lett.*, vol. 19, no. 1, pp. 178–182, Jan. 2020.
- [8] J. Zhu, Y. Yang, S. Liao, and Q. Xue, "Dual-band antenna hybridizing folded transmitarray and folded reflectarray," *IEEE Trans. Antennas Propag.*, vol. 70, no. 4, pp. 3070–3075, Apr. 2022.
- [9] G. Trentini, "Partially reflecting sheet arrays," *IRE Trans. Antennas Propag.*, vol. 4, no. 4, pp. 666–671, Oct. 1956.
- [10] D. Jackson and N. Alexopoulos, "Gain enhancement methods for printed circuit antennas," *IEEE Trans. Antennas Propag.*, vol. 33, no. 9, pp. 976–987, Sep. 1985.

- [11] Y. J. Lee, J. Yeo, R. Mittra, and W. S. Park, "Application of electromagnetic bandgap (EBG) superstrates with controllable defects for a class of patch antennas as spatial angular filters," *IEEE Trans. Antennas Propag.*, vol. 53, no. 1, pp. 224–235, Jan. 2005.
- [12] A. P. Feresidis and J. C. Vardaxoglou, "High gain planar antenna using optimised partially reflective surfaces," *IEE Microw. Antennas Propag.*, vol. 148, no. 6, pp. 345–350, Dec. 2001.
- [13] R. M. Hashmi and K. P. Esselle, "A class of extremely wideband resonant cavity antennas with large directivity-bandwidth products," *IEEE Trans. Antennas Propag.*, vol. 64, no. 2, pp. 830–835, Feb. 2016.
- [14] F. Wu and K. M. Luk, "Wideband high-gain open resonator antenna using a spherically modified, second-order cavity," *IEEE Trans. Antennas Propag.*, vol. 65, no. 4, pp. 2112–2116, Apr. 2017.
- [15] M. W. Niaz, Y. Yin, R. A. Bhatti, Y.-M. Cai, and J. Chen, "Wideband Fabry–Perot resonator antenna employing multilayer partially reflective surface," *IEEE Trans. Antennas Propag.*, vol. 69, no. 4, pp. 2404–2409, Apr. 2021.
- [16] F. Deng and J. Qi, "Shrinking profile of Fabry–Perot cavity antennas with stratified metasurfaces: Accurate equivalent circuit design and broadband high-gain performance," *IEEE Antennas Wireless Propag. Lett.*, vol. 19, pp. 208–212, 2020.
- [17] M. Thevenot, C. Cheype, A. Reineix, and B. Jecko, "Directive photonic-bandgap antennas," *IEEE Trans. Microw. Theory Techn.*, vol. 47, no. 11, pp. 2115–2122, Nov. 1999.
- [18] A. R. Weily, K. P. Esselle, B. C. Sanders, and T. S. Bird, "High-gain 1D EBG resonator antenna," *Microw. Opt. Technol. Lett.*, vol. 47, no. 2, pp. 107–114, 2005.
- [19] H. Yang and N. Alexopoulos, "Gain enhancement methods for printed circuit antennas through multiple superstrates," *IEEE Trans. Antennas Propag.*, vol. 35, no. 7, pp. 860–863, Jul. 1987.
- [20] N. Nguyen-Trong, H. H. Tran, T. K. Nguyen, and A. M. Abbosh, "A compact wideband circular polarized Fabry–Perot antenna using resonance structure of thin dielectric slabs," *IEEE Access*, vol. 6, pp. 56333–56339, 2018.
- [21] M. A. Al-Tarifi, D. E. Anagnostou, A. K. Amert, and K. W. Whites, "Bandwidth enhancement of the resonant cavity antenna by using two dielectric superstrates," *IEEE Trans. Antennas Propag.*, vol. 61, no. 4, pp. 1898–1908, Apr. 2013.
- [22] R. M. Hashmi, B. A. Zeb, and K. P. Esselle, "Wideband high-gain EBG resonator antennas with small footprints and all dielectric superstructures," *IEEE Trans. Antennas Propag.*, vol. 62, no. 6, pp. 2970–2977, Jun. 2014.
- [23] N. Wang, J. Li, G. Wei, L. Talbi, Q. Zeng, and J. Xu, "Wideband Fabry–Perot resonator antenna with two layers of dielectric superstrates," *IEEE Antennas Wireless Propag. Lett.*, vol. 22, pp. 229–232, 2015.
- [24] Y. Ge, K. P. Esselle, and T. S. Bird, "The use of simple thin partially reflective surfaces with positive reflection phase gradients to design wideband, low-profile EBG resonator antennas," *IEEE Trans. Antennas Propag.*, vol. 60, no. 2, pp. 743–750, Feb. 2012.
- [25] N. Wang, Q. Liu, C. Wu, L. Talbi, Q. Zeng, and J. Xu, "Wideband Fabry–Perot resonator antenna with two complementary FSS layers," *IEEE Trans. Antennas Propag.*, vol. 62, no. 5, pp. 2463–2471, May 2014.
- [26] K. Konstantinidis, A. P. Feresidis, and P. S. Hall, "Broadband sub-wavelength profile high-gain antennas based on multi-layer metasurfaces," *IEEE Trans. Antennas Propag.*, vol. 63, no. 1, pp. 423–427, Jan. 2015.
- [27] A. Weily, L. Horvath, K. Esselle, B. Sanders, and T. Bird, "A planar resonator antenna based on a woodpile EBG material," *IEEE Trans. Antennas Propag.*, vol. 53, no. 1, pp. 216–223, Jan. 2005.
- [28] D. Jackson and A. Oliner, "A leaky-wave analysis of the high-gain printed antenna configuration," *IEEE Trans. Antennas Propag.*, vol. 36, no. 7, pp. 905–910, Jul. 1988.
- [29] C. Cheype, C. Serier, M. Thevenot, T. Monediere, A. Reineix, and B. Jecko, "An electromagnetic bandgap resonator antenna," *IEEE Trans. Antennas Propag.*, vol. 50, no. 9, pp. 1285–1290, Sep. 2002.
- [30] L. Leger, T. Monediere, and B. Jecko, "Enhancement of gain and radiation bandwidth for a planar 1-D EBG antenna," *IEEE Microw. Wireless Compon. Lett.*, vol. 15, no. 9, pp. 573–575, Sep. 2005.
- [31] R. Gardelli, M. Albani, and F. Capolino, "Array thinning by using antennas in a Fabry–Perot cavity for gain enhancement," *IEEE Trans. Antennas Propag.*, vol. 54, no. 7, pp. 1979–1990, Jul. 2006.
- [32] A. R. Weily, K. Esselle, T. S. Bird, and B. C. Sanders, "Dual resonator 1-D EBG antenna with slot array feed for improved radiation bandwidth," *IET Microw. Antennas Propag.*, vol. 1, no. 1, pp. 198–203, 2007.
- [33] L. Moustafa and B. Jecko, "Design of a wideband highly directive EBG antenna using double-layer frequency selective surfaces and multifeed technique for application in the ku-band," *IEEE Antennas Wireless Propag. Lett.*, vol. 9, pp. 342–346, 2010.
- [34] C. Mateo-Segura, A. P. Feresidis, and G. Goussetis, "Bandwidth enhancement of 2-D leaky-wave antennas with double-layer periodic surfaces," *IEEE Trans. Antennas Propag.*, vol. 62, no. 2, pp. 586–593, Feb. 2014.
- [35] F. Qin et al., "Wideband circularly polarized Fabry–Perot antenna [antenna applications corner]," *IEEE Antennas Propag. Mag.*, vol. 57, no. 5, pp. 127–135, Oct. 2015.
- [36] R. M. Hashmi, B. A. Zeb, and K. P. Esselle, "Wideband high-gain EBG resonator antennas with small footprints and all-dielectric superstructures," *IEEE Trans. Antennas Propag.*, vol. 62, no. 6, pp. 2970–2977, Jun. 2014.
- [37] A. Baba, R. Hashmi, and K. Esselle, "Wideband gain enhancement of slot antenna using superstructure with optimised axial permittivity variation," *Electron. Lett.*, vol. 52, no. 4, pp. 266–268, 2016.
- [38] N. Wang, L. Talbi, Q. Zeng, and J. Xu, "Wideband Fabry–Perot resonator antenna with electrically thin dielectric superstrates," *IEEE Access*, vol. 6, pp. 14966–14973, 2018.
- [39] A. A. Baba, R. M. Hashmi, K. P. Esselle, and A. R. Weily, "Compact high-gain antenna with simple all-dielectric partially reflecting surface," *IEEE Trans. Antennas Propag.*, vol. 66, no. 8, pp. 4343–4348, Aug. 2018.
- [40] Z.-H. Wu and W.-X. Zhang, "Broadband printed compound air-fed array antennas," *IEEE Antennas Wireless Propag. Lett.*, vol. 9, pp. 187–190, 2010.
- [41] L.-Y. Ji, P.-Y. Qin, and Y. J. Guo, "Wideband Fabry–Perot cavity antenna with a shaped ground plane," *IEEE Access*, vol. 6, pp. 2291–2297, 2018.
- [42] T. A. Khan and A. M. H. Wong, "Wideband high-gain open resonator antenna using a flat impedance surface," in *Proc. IEEE Int. Symp. Antennas Propag. USNC-URSI Radio Sci. Meeting (APS/URSI)*, 2021, pp. 1966–1967.
- [43] P. Li, T. A. Khan, and A. M. H. Wong, "A wideband high-gain resonator cavity antenna with 2-level stepped ground," in *Proc. IEEE Asia Pac. Microw. Conf. (APMC)*, 2021, pp. 196–198.
- [44] Q.-Y. Guo and H. Wong, "Wideband and high-gain Fabry–Pérot cavity antenna with switched beams for millimeter-wave applications," *IEEE Trans. Antennas Propag.*, vol. 67, no. 7, pp. 4339–4347, Jul. 2019.
- [45] Q.-Y. Guo, Q. W. Lin, and H. Wong, "A high gain millimeter-wave circularly polarized Fabry–Pérot antenna using PRS-integrated polarizer," *IEEE Trans. Antennas Propag.*, vol. 69, no. 2, pp. 1179–1183, Feb. 2021.
- [46] S. M. A. Momeni Hasan Abadi, K. Ghaemi, and N. Behdad, "Ultra-wideband, true-time-delay reflectarray antennas using ground-plane-backed, miniaturized-element frequency selective surfaces," *IEEE Trans. Antennas Propag.*, vol. 63, no. 2, pp. 534–542, Feb. 2015.
- [47] L. Liang and S. Victor Hum, "Design of a UWB reflectarray as an impedance surface using Bessel filters," *IEEE Trans. Antennas Propag.*, vol. 64, no. 10, pp. 4242–4255, Oct. 2016.
- [48] L. D. Paarmann, *Design and Analysis of Analog Filters: A Signal Processing Perspective*, vol. 617. New York, NY, USA: Springer, 2006.
- [49] W. Thomson, "Delay networks having maximally flat frequency characteristics," *IEE Part-III Radio Commun. Eng.*, vol. 96, no. 44, pp. 487–490, 1949.
- [50] M. Li, M. A. Al-Joumayly, and N. Behdad, "Broadband true-time-delay microwave lenses based on miniaturized element frequency selective surfaces," *IEEE Trans. Antennas Propag.*, vol. 61, no. 3, pp. 1166–1179, Mar. 2013.
- [51] H. Delafkar and A. Pirhadi, "An accurate method for synthesis of reflecting elements to design wideband reflectarray antenna," *IEEE Trans. Antennas Propag.*, vol. 66, no. 5, pp. 2392–2400, May 2018.
- [52] N. Behdad, "A review of recent advances in designing true-time-delay microwave lenses exploiting metamaterials with non-resonant constituting unit cells," *Appl. Comput. Electromagn. Soc. J.*, vol. 29, no. 12, pp. 934–943, 2014.

- [53] J. Budhu and A. Grbic, "Perfectly reflecting metasurface reflectarrays: Mutual coupling modeling between unique elements through homogenization," *IEEE Trans. Antennas Propag.*, vol. 69, no. 1, pp. 122–134, Jan. 2021.
- [54] J. Cheng and H. Mosallaei, "Truly achromatic optical metasurfaces: A filter circuit theory-based design," *J. Opt. Soc. Amer. B*, vol. 32, no. 10, pp. 2115–2121, 2015.
- [55] J. P. S. Wong, M. Selvanayagam, and G. V. Eleftheriades, "Polarization considerations for scalar Huygens metasurfaces and characterization for 2-D refraction," *IEEE Trans. Microw. Theory Techn.*, vol. 63, no. 3, pp. 913–924, Mar. 2015.
- [56] O. Luukkonen et al., "Simple and accurate analytical model of planar grids and high-impedance surfaces comprising metal strips or patches," *IEEE Trans. Antennas Propag.*, vol. 56, no. 6, pp. 1624–1632, Jun. 2008.
- [57] J. Wong, M. Selvanayagam, and G. V. Eleftheriades, "A thin printed metasurface for microwave refraction," in *Proc. IEEE MTT-S Int. Microw. Symp. (IMS)*, 2014, pp. 1–4.
- [58] A. A. Fathnan and D. A. Powell, "Bandwidth and size limits of achromatic printed-circuit metasurfaces," *Opt. Exp.*, vol. 26, no. 22, pp. 29440–29450, 2018.
- [59] A. E. Olk, P. E. M. Macchi, and D. A. Powell, "High-efficiency refracting millimeter-wave metasurfaces," *IEEE Trans. Antennas Propag.*, vol. 68, no. 7, pp. 5453–5462, Jul. 2020.
- [60] A. E. Olk, M. Liu, and D. A. Powell, "Printed tapered leaky-wave antennas for W-band frequencies," *IEEE Trans. Antennas Propag.*, vol. 70, no. 2, pp. 900–910, Feb. 2022.
- [61] C. Pfeiffer and A. Grbic, "Metamaterial Huygens' surfaces: Tailoring wave fronts with reflectionless sheets," *Phys. Rev. Lett.*, vol. 110, no. 19, 2013, Art. no. 197401.
- [62] R. M. Hashmi, K. Esselle, B. Zeb, and S. G. Hay, "Electromagnetic band gap (EBG) resonator antennas with high aperture efficiencies," in *Proc. Int. Conf. Electromagn. Adv. Appl. (ICEAA)*, 2014, pp. 624–627.
- [63] A. A. Baba, R. M. Hashmi, and K. P. Esselle, "Achieving a large gain-bandwidth product from a compact antenna," *IEEE Trans. Antennas Propag.*, vol. 65, no. 7, pp. 3437–3446, Jul. 2017.



**ALEX M. H. WONG** (Senior Member, IEEE) received the B.A.Sc. degree in engineering science (electrical option) and the M.A.Sc. and Ph.D. degrees in electrical and computer engineering from the University of Toronto, Canada, in 2006, 2009, and 2014, respectively.

He then served briefly as a Postdoctoral Fellow with the University of Toronto. Since 2018, he has been an Assistant Professor of Applied Electromagnetics with the Department of Electronic Engineering, City University of Hong

Kong, Hong Kong, where he is also a member of the State Key Laboratory of Terahertz and Millimeter Waves. He has advanced multiple projects in applied electromagnetics on next-generation RF, infrared and optical metasurfaces, and super-resolution imaging and radar systems. Particularly, he has made academic contributions to research on wave shaping using Huygens' metasurfaces and far-field imaging based on super-oscillation waves. His current research interests include metasurfaces, metamaterials, and super-resolution systems. His received accolades include an IEEE RWP King Award (for the best annual publication by a young author in the IEEE TRANSACTIONS ON ANTENNAS AND PROPAGATION), the URSI Young Scientist Award, the Raj Mittra Grant, the IEEE Doctoral Research Awards from the AP and MTT societies, and the Canada Graduate Scholarship (doctoral level). He serves as the TPC Vice-Chair for the 2020 Asia-Pacific Microwave Conference. He has taken on various programme committee, session chair and technical judge and reviewer duties for IEEE conferences and journal publications in the AP and MTT societies, as well as relevant venues in applied physics. He is a member of the IEEE Antennas and Propagation Society, Microwave Theory and Techniques Society and the Photonics Society.



**TAYYAB A. KHAN** (Member, IEEE) received the M.S. degree in information and communication engineering from the Electromagnetics and Communication Laboratory, Xi'an Jiaotong University, Xi'an, China, in 2019. He is currently pursuing the Ph.D. degree in electrical engineering from the City University of Hong Kong, Hong Kong. His current research interests include the development of meta-surfaces for antenna systems.